Brain Stimulation 15 (2022) 624–634

Contents lists available at ScienceDirect

Brain Stimulation

journal homepage: http://www.journals.elsevier.com/brain-stimulation

Selective augmentation of corticospinal motor drive with trans-spinal direct current stimulation in the cat

Preston T.J.A. Williams [a, **], Dennis Q. Truong [b], Alan C. Seifert [c], Junqian Xu [d], Marom Bikson [b], John H. Martin [a, e, *]

[a] Department of Molecular, Cellular and Biomedical Sciences, CUNY School of Medicine, New York, NY, USA
[b] Department of Biomedical Engineering, The City College of New York, NY, USA
[c] BioMedical Engineering and Imaging Institute, Department of Radiology, And Graduate School of Biomedical Sciences, Icahn School of Medicine at Mount Sinai, New York, NY, USA
[d] Departments of Radiology and Psychiatry, Baylor College of Medicine, Houston, TX, USA
[e] The Graduate Center, City University of New York, NY, USA

ARTICLE INFO

Article history:
Received 10 January 2022
Received in revised form
26 March 2022
Accepted 27 March 2022
Available online 31 March 2022

Keywords:
Neuromodulation
Corticospinal
Spinal cord
Motor-evoked potential
Motoneuron
Finite element method
Electric field
Large-animal model

ABSTRACT

Background: A key outcome for spinal cord stimulation for neurorehabilitation after injury is to strengthen corticospinal system control of the arm and hand. Non-invasive, compared with invasive, spinal stimulation minimizes risk but depends on muscle-specific actions for restorative functions.
Objective: We developed a large-animal (cat) model, combining computational and experimental techniques, to characterize neuromodulation with transcutaneous spinal direct current stimulation (tsDCS) for facilitation of corticospinal motor drive to specific forelimb muscles.
Methods: Acute modulation of corticospinal function by tsDCS was measured using motor cortex-evoked muscle potentials (MEPs). The effects of current intensity, polarity (cathodal, anodal), and electrode position on specific forelimb muscle (biceps vs extensor carpi radialis, ECR) MEP modulation were examined. Locations of a key target, the motoneuron pools, were determined using neuronal tracing. A high-resolution anatomical (MRI and CT) model was developed for computational simulation of spinal current flow during tsDCS.
Results: Effects of tsDCS on corticospinal excitability were robust and immediate, therefore supporting MEPs as a sensitive marker of tsDCS targeting. Varying cathodal/anodal current intensity modulated MEP enhancement/suppression, with higher cathodal sensitivity. Muscle-specificity depended on cathode position; the rostral position preferentially augmented biceps responses and the caudal position, ECR responses. Precise anatomical current-flow modeling, supplemented with target motor pool distributions, can explain tsDCS focality on muscle groups.
Conclusion: Anatomical current-flow modeling with physiological validation based on MEPs provides a framework to optimize muscle-specific tsDCS interventions. tsDCS targeting of representative motor pools enables muscle- and response-specific neuromodulation of corticospinal motor drive.

1. Introduction

A key outcome for spinal cord neurorehabilitation is to enhance function of the corticospinal system after injury because of its necessary role in voluntary control of the arm and hand [1,2]. The motor cortex (MCX), the principal origin of the corticospinal tract (CST), is one target for stimulation-based restorative therapies after stroke and spinal cord injury [3–5] and can promote function after

Abbreviations: CST, corticospinal tract; ECR, extensor carpi radialis; FEM, finite element method; MCX, primary motor cortex; MEP, motor-evoked potential; MT, motor threshold; tsDCS, transcutaneous spinal direct current stimulation [c-tsDCS (cathodal) and a-tsDCS (anodal), respectively.

* Corresponding author. Department of Molecular, Cellular, and Biomedical Sciences City University of New York School of Medicine & Center for Discovery and Innovation, 160 Convent Avenue, New York, NY, 10031, USA.
** Corresponding author.
E-mail addresses: pwilliams@ccny.cuny.edu (P.T.J.A. Williams), jmartin@med.cuny.edu (J.H. Martin).

https://doi.org/10.1016/j.brs.2022.03.007

a brain injury [6]. MCX stimulation can steer representational plasticity [7] and promote CST structural remodeling [6,8]. An alternative stimulation target is the spinal cord [3,9,10], to activate intrinsic spinal circuits to promote the strength and fidelity of CST transmission. Transcutaneous spinal direct current stimulation (tsDCS) is a non-invasive approach for neuromodulation of spinal cord networks that can augment corticospinal system output, including MCX-evoked spinal synaptic responses [11] and MEPs [12,13]. tsDCS modulates MEPs in most studies (cf, however [14]) and is well-tolerated in human trials [15–17]. It is adjustable and cost-effective because it is non-invasive. Use of a direct current waveform allows bidirectional (excitation/inhibition) neuromodulation [18–21] based on electrode polarity (cathodal/anodal). Whereas most studies showed that c-tsDCS augments muscle activity evoked by motor cortex stimulation and a-tsDCS either has a minimal effect or suppresses activity (e.g. Refs. [20–23], other studies have shown minimal differences between a- and c-tsDCS (e.g., Ref. [24]) or dominant anodal facilitation (e.g., Refs. [25–27]). Selecting tsDCS intensity and polarity, along with adjusting surface electrode positions to steer current to the spinal cord, offers the potential to customize resulting neuromodulation and plasticity after injury. However, clinical optimization of tsDCS requires a better understanding about how tsDCS targets spinal segments and impacts muscle response strength.

The overall objective of this study was to characterize neuromodulation with tsDCS for facilitation of corticospinal drive to specific arm muscles (biceps or extensor carpi radialis, ECR). To this end, we developed a large-animal (cat) model to study segmental localization, muscle-effect targeting, and clinical translation. tsDCS, like transcranial direct current stimulation (tDCS) for the brain, applies low-intensity direct current through electrodes on the skin to polarize underlying neural structures, leading to changes in local synaptic and network activity [11,28–30]. Like all forms of neuromodulation, tsDCS 'dose'—defined as the electrode montage, current intensity, and polarity—governs the spatial characteristics of current flow to target neural elements [31] and the resulting neuromodulation. The details of the underlying anatomy shape current flow patterns, which can be predicted by Finite Element Method (FEM) simulations [32,33]. In this study, a novel MRI/CT-derived model of intra-spinal current flow integrated with segmental neuronal morphology and connectivity data were evaluated in relation to evoked physiological measurements to investigate tsDCS mechanisms of action. We measured modulation of MCX-evoked corticospinal output (MEPs) in two forelimb muscles during cervico-thoracic tsDCS. We show that tsDCS acts immediately to modulate MEPs. Differential cathode positioning produced preferential augmentation of either biceps or ECR responses; which was explained by montage-specific segmental current flow and the rostrocaudal distributions of their respective motor pools. Our findings demonstrate tsDCS targeting of representative motor pools for proximal and distal muscles, thereby enabling muscle- and response-specific neuromodulation to boost muscle strength which is significant for efficacious neurorehabilitation.

2. Methods

2.1. Subjects and general procedures

Experimental procedures were approved by and conducted in accordance with the Institutional Animal Care and Use Committee of the Advanced Science Research Center of the City University of New York. Cats were obtained from an Association for Assessment and Accreditation of Laboratory Animal Care International (AAALAC)-accredited supplier and housed in a controlled vivarium with food and water available ad libitum. The minimum number of animals necessary to complete the experiments were used and care was taken to reduce any pain or discomfort. The number of animals in each group to complete the studies was (imaging n = 2; tsDCS intensity/polarity n = 4; motor neuron pools n = 2; tsDCS montage n = 3). One animal in the tsDCS montage group was used, after completing the MEP recordings, to study MN pools (total = 10 cats).

For surgical procedures to implant the MCX epidural electrode, a broad-spectrum antibiotic (cefazolin, 25 mg/kg i.m.), an analgesic (buprenorphine, 0.02 mg/kg i.m.), and an antimuscarinic (glycopyrrolate, 0.11 mg/kg i.m.), were administered prior to induction. Anesthesia was induced with acepromazine (0.03 mg/kg i.m.) and ketamine hydrochloride (30 mg/kg i.m.), and maintained with isoflurane (1.5–3% in oxygen). Fluids were supplemented with lactated Ringer's and body temperature maintained at 38 °C. Surgeries were performed under aseptic conditions. For electrophysiology experiments, anesthesia was maintained with continuous infusion of ketamine (10 mg/kg/h i.v.) [34]. For MCX electrode implantation, the head was fixed in a stereotaxic frame and craniotomies were made to expose the dura overlaying MCX bilaterally. Electrode placement was guided by the effects of stimulation to evoke contralateral elbow- and wrist-joint movements. In the tsDCS montage group, the electrode and a connector were secured into position with an acrylic headcap and the recordings were performed during a separate procedure. Antibiotics (cefazolin, 25 mg/kg i.m.), analgesics (buprenorphine, 0.02 mg/kg i.m; meloxicam, 0.3 mg/kg, s.c.), and fluids were administered post-surgically.

2.2. EMG recording and signal processing

Indwelling percutaneous electrodes were fabricated from insulated stainless steel or tungsten fine wire (0.004' diameter, California Fine Wire, USA) and prepared with a deinsulated hook (1–1.5 mm) at the tip. An electrode pair was inserted 2–3 mm apart for differential EMG recordings. Single-pulse biphasic muscle stimulation confirmed contraction of the target muscles (biceps brachii; external carpi radialis, ECR) and recording of passive joint movement. The EMG signals were bandpass filtered between 300 and 5000 Hz, amplified (A-M Systems, USA), and digitized (Power 1401, CED, UK) with a 10 kHz sampling frequency for offline analysis (Signal, CED, UK). Trials were screened and removed from analysis if contaminated by electrical or movement artifacts.

2.3. Motor evoked potential (MEP) testing

The epidural MCX (Fig. 1A) electrode was made of a pair of insulated stainless steel wires (PTechnologies, USA), deinsulated at the end (2–3 mm; 1.5–2.0 mm separation) and contoured to the cortical curvature. The electrode was placed over the forelimb (coronal gyrus, area 4γ, [35,36]) region of M1 and lowered to appose the cortical surface and minimize current shunting through the CSF. We delivered trains of biphasic pulses (3 or 7 pulses; 0.02 ms; 333 Hz) using an isolated stimulation unit (A-M Systems) to produce a single muscle evoked potential (MEP; Fig. 1C). Epidural stimulation was repeated once every 2 s for 20 trials. The motor threshold (MT) was defined as the minimum amount of current to evoke a MEP on 90% of trials. Biceps and ECR muscle responses are the most common muscle responses evoked epidurally over the forelimb cortex, with ECR MEPs occurring within 0.8 mA of biceps MEPs. Muscle recruitment was performed at threshold, 1.2, and 1.4 MT. Custom scripts (Signal, CED) were used to subtract the mean background activity (50 ms sample before the stimulus) in each trial (sweep) prior to the first stimulation train. In all animals, MEPs were measured as the rectified integrated area of EMG activity

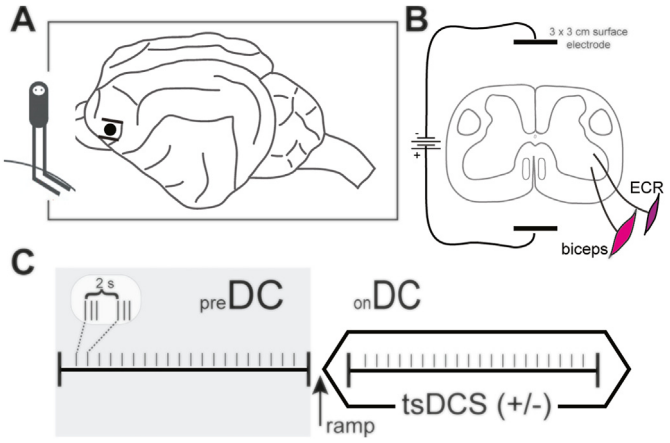

Fig. 1. Approach to assess tsDCS neuromodulation of the corticospinal system in a large animal model. A. Schematic of cortical stimulation to test motor-evoked potentials (MEPs) in cat. The forelimb representation of the motor cortex (over the cruciate sulcus, inset) was electrically stimulated epidurally to evoke EMG responses. **B**. Schematic of tsDCS to examine modulation of MEP responses for biceps and ECR muscles. The tsDCS target electrode was placed on the dorsal midline and was moved for montage comparisons; the return electrode was placed ventrally on the manubrium. **C**. Stimulation protocols. MEPs were generated with a stimulation train (3 pulses, 333 Hz; 0.2 ms; 2 s repeat; 20 trials) before tsDCS (baseline $_{pre}$DC, shaded) and during tsDCS ($_{on}$DC), following ramp (arrow).

within a 30 ms time window beginning 20 ms after the first stimulation pulse.

2.4. tsDCS and electrode montages

tsDCS was administered using a dorsal and ventral electrode (target and return electrode, respectively; Fig. 1B) [12]. We used a tsDCS montage to deliver current flow to the rostral cervical enlargement based on parallel studies examining tsDCS neuromodulation therapy for cervical spinal cord injury [37]. The dorsal electrode spanned C2–C6 and the ventral electrode placed on the sternal manubrium. In later experiments to assess electrode montage focality, the dorsal electrode spanned T2-T6 (caudal); the ventral electrode was also placed on the sternal manubrium.

We used a commercially available isolated stimulation unit (Model 0707A, Soterix Medical, USA) to deliver tsDCS. Pairs of surface electrodes (3 × 3 cm) were made from hydrogel electrodes (PALS, North Coast Medical, USA), or saline-soaked sponges activated by a carbon rubber insert in a silicone casing (Caputron, USA). The electrode size for cat stimulation was based on practical experimental and anatomical considerations to reduce current density at the electrode surface. The size is generally scaled down from human cases and up from our rat study [38]. The hair was trimmed and skin cleansed with isopropyl alcohol to reduce electrical resistance. The electrodes were placed on the midline and secured on the skin surface with straps. The duration of tsDCS typically was on for 40 s, with a 30 s ramp up and a 30 s ramp down period (Fig. 1B). Electrode contact quality and current delivery were continuously monitored; we did not find a difference between electrode materials. Baseline MEPs were measured immediately before tsDCS. Minor erythema was observed, lasting a few minutes, after tsDCS with no signs of tissue damage or petechiae.

2.5. Anatomical determination of motoneuron pools

Motoneuron distributions were determined for biceps and ECR muscles using retrograde tracing, as in our previous study [39]. Anesthesia was induced as above, and tracer (cholera toxin b-fragment, CTB; 1% in sterile water, 40–45 μl total volume; List Biological, USA) was injected using a microsyringe over a 3 min period. The needle was inserted parallel to the long axis of the muscle from distal to proximal approach into the muscle belly [40]. The muscle surface was rinsed with saline, the skin closed with sutures, and treated with topical antibiotics (in addition to above). Terminal procedures were performed one week later to extract the spinal cord. The animal was deeply anesthetized (Sodium Pentobarbitol, 30 mg/kg) for transcardial-perfusion with saline followed by 4% paraformaldehyde. The dorsal root ganglia and entry zones were examined while the cord was in the dural sac for accurate segmental identification. Tissue blocks (C2-T2) were dissected, post-fixed in 4% paraformaldehyde, and then cryoprotected in 20% sucrose solution at 4 °C. Frozen sections (40 μm) were cut. CTB staining was performed using a goat anti-CTB (1:1000; List Biologicals, USA) primary antibody and a donkey anti-goat secondary antibody conjugated to FITC. The number of CTB-labeled motoneuron somas for each muscle group in the same sections were counted. We sampled 20 sections/segment, with a wide sampling interval of approximately 1 section in every 0.4 mm for a total volume of 8.0 mm^2.

2.6. Finite element method modeling

High resolution Magnetic Resonance Imaging (MRI, Magnetom Skyra 3T, Siemens, Erlangen, Germany) and Computerized Tomography (CT, Somatom Force, Siemens, Erlangen, Germany) scans were acquired to construct a finite element method (FEM) model of the feline spinal cord and surrounding tissues. We used post-mortem animals (n = 2) to eliminate movement artifacts and achieve full-body coverage in T_1-weighted 3D magnetization-prepared rapid gradient-echo (MP-RAGE) and T_2-weighted 3D variable flip-angle turbo spin-echo (TSE) scans at 0.67 mm isotropic resolution. An additional proton density-weighted 2D gradient-echo (GRE) scan was acquired at 0.3 mm in-plane resolution and 2.5 mm slice thickness with more limited rostral-caudal coverage of the spinal cord to enhance contrast between white and gray matter. Full body CT scans at 0.3–0.5 mm isotropic resolution were acquired to distinguish bone from air-filled cavities. MR and CT imaging volumes were co-registered with an image processing toolbox (3D Slicer). Tissues for which electrical conductivity values were to be assigned were segmented, including skin, fat, muscle, bone, intervertebral disks, cerebrospinal fluid (CSF), gray matter, white matter, air, and sinus cavities. Manual segmentation was carefully performed to avoid errors due to residual image artifacts, ensure continuity of tissue layers, and refine relevant anatomy. The electrodes used for tsDCS simulations were added to the model with a mesh-to-voxel software (ScanIP + CAD) to generate Computer Aided Design-generated sponges (3 × 3 cm) on the skin surface.

We used the computational FEM to model tsDCS and simulate current density. Adaptive tetrahedral meshes were generated with a voxel-based meshing algorithm (ScanIP + FE) for FEM modeling (COMSOL). Electrostatic volume conductor physics [field equation: $(\nabla\cdot(\sigma\nabla V) = 0)$] and electrical conductivities (in S/m) were applied [Skin, 0.465; fat 0.025; muscle, 0.2; bone, 0.01; CSF or fluid, 1.65; gray matter, 0.276; white matter, 0.126; air, 1e-6; saline sponge, 1.4; based on [41,42]]. Inward current (1 mA) and ground (V = 0) boundary conditions were applied at the anode and cathode respectively. The intensity of electrical stimulation was derived by linearly scaling the resulting field equation. FEM maps of current density and electric field were calculated for the whole volume model. The hindquarters and lumbar cord had little/no impact on the solved models and were truncated to emphasize the current density magnitude across the cervicothoracic axis. Inter-segmental differences were further compared by estimating the mean across

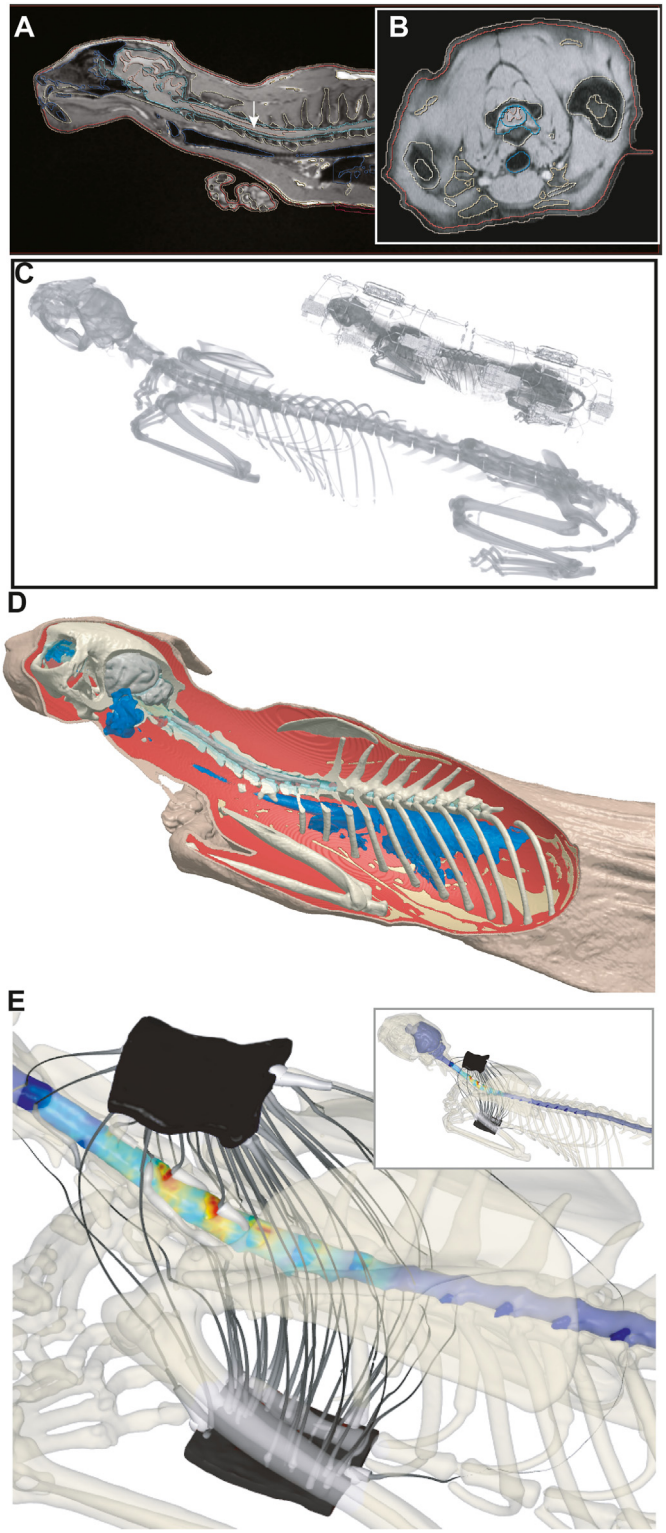

Fig. 2. Workflow for Finite Element Method (FEM) computational modeling. Co-registration and segmentation of the whole-body multi-image model. **A**. Representative image of tissue elements at midsagittal (MR-T1-weighted); and **B**. transverse (MR-proton density-weighted) planes. Examples of tissue segmentation are shown in the MRI scans (light blue = CSF; dark blue = major cavities; yellow = bone). The white arrow in the midsagittal image (A) marks the plane of the transverse image (B). **C**. Skeletal bone detail (CT; inset shows MRI radiofrequency coil positions). **D**. Rendering of the realistic whole-body model. **E**. FEM model of the electric fields (black lines) generated between the dorsal (target) and ventral (return) cutaneous electrodes (black flux squares). The proportional magnitude of electric current in the spinal cord is represented as a density colormap (low = blue; high = red). The illustration is for the rostral-tsDCS montage (inset). (For interpretation of the references to color in this figure legend, the reader is referred to the Web version of this article.)

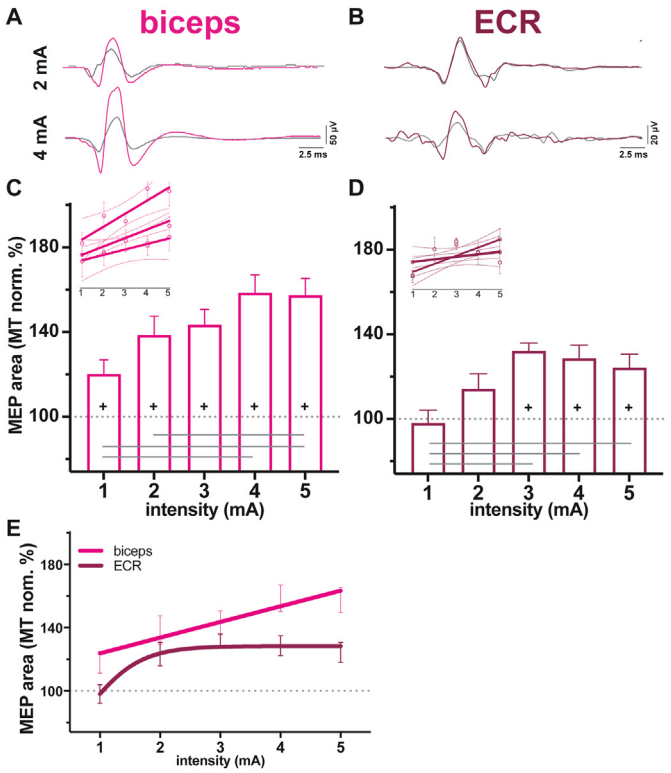

Fig. 3. Cathodal tsDCS augments MEP size.
A and B. Representative MEP responses for the biceps (**A**) and ECR (**B**) in the same animal before (preDC, black trace) and during 2 mA or 4 mA tsDCS (top and bottom, respectively; traces averaged and smoothed). **C and D**. Intensity-dependent neuromodulation of MEP area. Biceps responses (C) showed augmentation above baseline (1.0 MT, dotted line) with each intensity, whereas ECR (D) increased with 3 mA and above (' + '; mean ± SEM). Generally, higher intensities of tsDCS produced larger MEPs than lower doses (horizontal lines connect differences between bars). The insets show linear regressions for individual subject data (symbol error bars ± SEM; regression error bands ± 95% C.I.). **E**. Curve-fit for tsDCS intensity on MEP responses. A linear fit was robust for biceps and a sigmoidal fit was better for ECR (symbol error bars ± SEM)].

white and gray matter components of slices extracted in the transverse plane. Focality was calculated by extracting adjoining slices (0.5 mm X 5 slices) centered on the peak magnitude in C4 and C8 segments. Our workflow adopted best practices from prior image-derived tsDCS models in humans and our prior study in the rat [33,43–45].

2.7. Statistical analyses

Statistical comparisons were performed with Prism 9.2 (Graphpad, USA). Variability between animals was examined with regression analyses to compare slopes and intercepts. Changes in the EMG response from baseline in each condition were detected with one-sample t-tests. Differences between conditions were compared with Mann-Whitney (MW) or Kruskal-Wallis (KW). Post hoc tests were performed using Bonferroni or Dunn's methods with alpha adjustments to control for familywise error. Mixed-model effects were analyzed with two-way ANOVA and Holm-Sidak post hoc, and Welch's multiple comparisons with Holm-Sidak correction. Trends across conditions were explored with linear regression slope comparisons and curve fitting (Sy.x and R^2).

3. Results

3.1. Realistic whole-body cat model of tsDCS using MRI and CT

This is the first feline FEM model. tsDCS parameters were informed with FEM modeling using a realistic whole-body reconstruction from MRI and CT scans. Such models are standard tools informing the relationship between applied dose (intensity and electrode locations) and resulting current flow in target tissue [46]. There is enhanced model resolution through the use of co-registration of post-mortem CT and MRI (0.2–0.3 mm voxels). Representative MRI sections are shown with overlayed segmented tissue mask outlines (Fig. 2A; T1-weighted sagittal slice; Fig. 2B, proton density-weighted transverse slice) and bones from CT imaging (2C, coil locations are indicated in the inset). The rendering of the resulting segmented masks (Fig. 2D) shows the precise representation of tissues. The resulting FEM model of current flow (Fig. 2E) for the rostral electrode montage illustrates both the global current flow pattern (black flux lines) and the detailed current flow through the spinal cord (false color). The periodic regions of local current density maxima on the dorsal surface of the spinal cord reflect lower-impedance intervertebral spaces. No significant current flow reaches the brain or lower thoracic segments. The model predicts, with high spatial resolution, the spatial pattern and peak intensity of the current density produced within the spinal cord and peri-spinal tissues.

3.2. tsDCS neuromodulation of cortical motor output is rapid and current intensity-dependent

To assess the neuromodulatory effect of tsDCS on motor output we first compared the MEP responses from biceps and ECR muscles recorded before and during tsDCS applied through the rostral montage at different cathodal intensity (1–5 mA). Motor cortex stimulation evoked a MEP that corresponded to a multiphasic compound muscle action potential. Cathodal tsDCS produces an acute current-dependent change in MEPs, with both biceps (Fig. 3A) and ECR (Fig. 3B) output increasing with increased applied current (Fig. 3C and D). For each muscle group, neuromodulation intensity-response was quantified across animals for 1–5 mA.

For biceps, cathodal tsDCS applied through the rostral-montage significantly increased MEP amplitude above baseline at all intensities tested (Fig. 3C), notwithstanding differences in individual animal (inset) sensitivity [1 mA $t_{(46)} = 3.03$, $P < 0.01^{+}$; 2 mA $t_{(55)} = 4.32$, $P < 0.001^{+}$; 3 mA $t_{(33)} = 6.10$, $P < 0.001^{+}$; 4 mA $t_{(54)} = 6.97$, $P < 0.001^{+}$; 5 mA $t_{(45)} = 7.19$, $P < 0.001^{+}$]. There was a significant increase in biceps motor output enhancing with tsDCS intensity from 1 mA (~20% increase) through 4 mA (~50% increase), with no significant difference between from 4 mA to 5 mA [KW: $H = 19.79$, $P < 0.001$*; Dunn $1 < 4$, $1 < 5$, $2 < 5$].

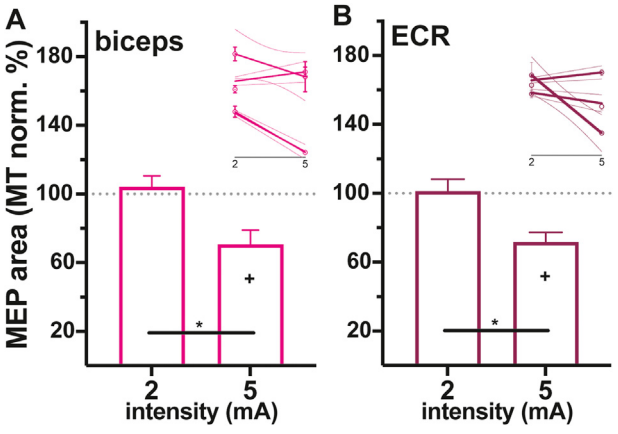

Fig. 4. Anodal tsDCS at high intensity reduced MEP area. The polarity of tsDCS was reversed with the rostral montage to determine dose-dependent neuromodulation with anodal tsDCS. MEP responses for biceps (A) and ECR (B) showed no change with a low intensity dose whereas using 5 mA reduced MEP area below baseline ('+'; mean ± SEM) and below the low dose ('*'). The inset shows regression plots for individual subject data (symbol error bars ± SEM; regression line ± 95% C.I.).

Cathodal tsDCS, through the same rostral montage, also increases ECR motor output, but a qualitatively different intensity-response than biceps output (Fig. 3D). Across animals, there was no significant increase above baseline in ECR output at 1 and 2 mA [1 mA $t_{(66)} = 0.31$; 2 mA $t_{(40)} = 2.02$, P's > 0.05]. Three mA tsDCS increased ECR MEPs by ~35%; 4–5 mA also increased ECR MEPs, but not more than 3 mA [3 mA $t_{(32)} = 8.61$; 4 mA $t_{(55)} = 4.58$; 5 mA $t_{(45)} = 3.88$; P's < 0.001^{+}; KW: $H = 35.71$, $P < 0.001$*; Dunn $1 < 3$, $1 < 4$, $1 < 5$]. In sum, tsDCS increased ECR motor output; however, the relative effect was smaller and saturated at a lower tsDCS intensity then biceps motor output.

The tsDCS average intensity response for biceps was well approximated by a linear fit (Fig. 3E, $R^2 = 0.89$; Sy.x = 6.28). The average intensity response for ECR was better fit by a sigmoid (Fig. 3E, Sy.x = 4.19) than a linear fit ($R^2 = 0.46$; Sy.x = 11.37). Multiple comparison between the change in response level indicates that biceps increases were greater with 1, 4 and 5 mA compared to ECR (Welch's with Holm-Sidak correction).

We further assessed if motor output augmentation by cathodal tsDCS (rostral montage) increases over time with tsDCS (i.e., 'wind-up') or if maximal modulation occurs immediately with the start of tsDCS. For biceps and ECR, regression slopes of pooled MEP responses across trials were flat during modulation by 2 or 5 mA tsDCS [$F_{(3,72)} = 0.67$, $P > 0.5$; pooled slope = −0.33], indicating that the MEPs were augmented rapidly and maintained. In summary, we observed rapid augmentation of MEP amplitude when tsDCS was applied and this enhanced response-level was sustained across trials.

3.3. Reversing polarity to anodal tsDCS suppressed the motor output at higher doses

We and others have previously shown that anodal DC stimulation can have opposite effects of cathodal stimulation, but with asymmetric sensitivity [13]. Modulation of biceps and ECR motor-output by anodal tsDCS was measured at low (2 mA) and high doses (5 mA). Using 2 mA stimulation (Fig. 4A and B), MEPs for biceps and ECR responses were not different from baseline [biceps $t_{(49)} = 0.15$; ECR $t_{(52)} = 0.19$, P's > 0.05]. Five mA anodal tsDCS significantly suppressed MEPs for biceps (Fig. 4A) and ECR (Fig. 4B) responses [biceps $t_{(48)} = 2.11$; ECR $t_{(55)} = 4.32$, P's < 0.05^{+}]. Sensitivity at anodal 5 mA was not significantly different between biceps (22% mean decrease) and ECR (28% mean decrease) [MW: U = 172, $P > 0.6$]. The degree of suppressed response during 5 mA was flat across trials for biceps and ECR [$F_{(1,35)} = 0.64$, $P > 0.4$; pooled slope = 0.47]. Individual animals responded similarly to anodal tsDCS (insets).

3.4. Motoneuron pool distributions predict differential montage targeting

MEP facilitation or suppression during tsDCS must involve a change in motoneuron recruitment (threshold, rate). We hypothesized that the increased sensitivity of tsDCS to augment the biceps more than the ECR the rostral montage is related to the rostro-caudal distribution of motoneuron cell bodies. We retrogradely traced biceps and ECR motoneurons and estimated the distribution

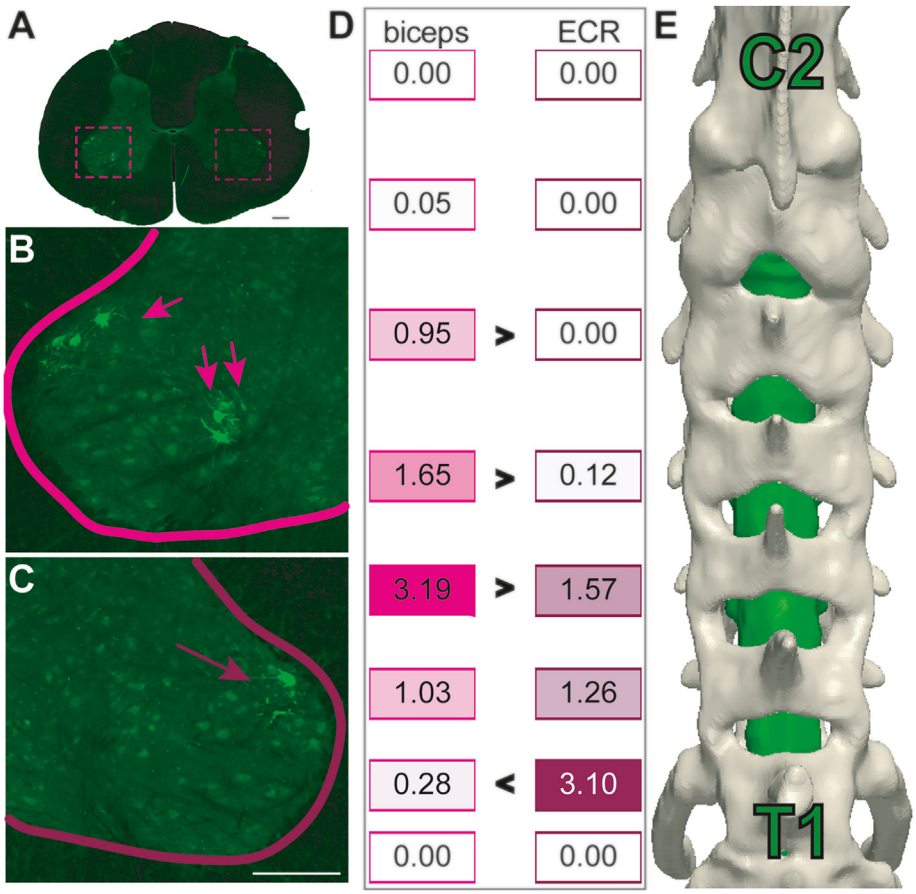

Fig. 5. Segmental distribution of motoneurons.
A. Micrograph of fluorescent-labeled motoneurons traced retrogradely from biceps (left) and ECR (right) in the same transverse section at C6. Expansion of the ventral horn illustrates the motoneuron somata for biceps (**B**) clustered primarily in a central region (double arrow), and occasionally clustered near the dorsolateral border (single arrow). ECR motoneurons (**C**) were only found clustered near the dorsolateral border (single arrow). **D**. Segmental distribution of motoneurons (mean value; shading indicates density) for biceps (left) and ECR (right). The biceps pool of motoneurons was more prevalent in rostral segments and the ECR was denser caudally (<>; indicates direction for significant differences). **E.** Model detail of the cervical column from the dorsal (posterior) perspective. The spinal cord (green) with the vertebrae (gray) were aligned with anatomical dissections of the spinal segments in D. *Calibrations in A, B, C*, 500 μm. (For interpretation of the references to color in this figure legend, the reader is referred to the Web version of this article.)

of labeled motoneuron pools (Fig. 5). A representative C6 micrograph (Fig. 5A) shows CTB-labeled biceps (5B) and ECR (5C) motoneurons. Biceps motoneurons were found predominately in a central region of the ventral horn (Fig. 5B, double arrows), consistent with prior reports in the cat [47]. Clusters, sometimes visualized in the same section (Fig. 5B, single arrow), were observed near the dorsolateral border of the ventral gray matter, abutting where the ECR motoneurons were observed (Fig. 5C, arrow). The density of the motor neuron pools (Fig. 5D, shading) indicates the biceps motoneurons were denser in rostral segments, whereas the ECR motoneurons were denser caudally. The density maps are aligned with a reconstruction of the cervical and upper thoracic spinal cord (Fig. 5E). There was an interaction between the density of soma for each muscle group and spinal segment [two-way ANOVA $F_{(5,482)} = 52.19$, $P < 0.001$; Bonferroni $C4^{\#}$: Biceps > ECR; $C5^{\#}$: Biceps > ECR; $C6^{\#}$: Biceps > ECR; $C8^{\#}$: Biceps < ECR; C3 and C7 n.s.]. At C3, we only found biceps motoneurons and the density was low. The biceps motor pool was more prevalent throughout C4–C6 and motoneuron density peaked at C6. The ECR pool was more caudal and motoneuron density peaked at C8.

3.5. Whole-body tsDCS computational maps reveal montage-dependent current focality

The forgoing analysis demonstrated a relatively larger effect of the rostral-montage cathodal tsDCS on biceps than ECR MEP enhancement and that this difference is associated with a more rostral biceps motor pool location than ECR. These findings suggest that the rostral cathode location may have selected for the rostrally-located biceps motoneurons and associated presynaptic circuits. We contrasted simulated spinal current density for the rostral montage (as tested above; Fig. 6 A1-3) with the caudal montage (Fig. 6 B1-3). With the rostral montage (Fig. 6 A1-3), tsDCS current density is higher rostrally (C4 segment) and lower caudally (C8 segment). Most of the spinal current flow (at >75% of peak) was restricted to approximately three segments from caudal C3 to rostral C6. tsDCS through the caudal montage produced maximal current flow (at >75% of peak) through C7, C8, and also in T1 (Fig. 6 B1-3). Note, the periodic modulation of current density corresponds to the vertebrae (reduced intraspinal current density) and intervertebral spaces (increased current density). Maps of the electric field magnitude (Fig. 6 A4,5; 6B4,5) show direction and predict areas of relative membrane polarization. Note that reversal of electrode polarity reverses the direction of current flow across

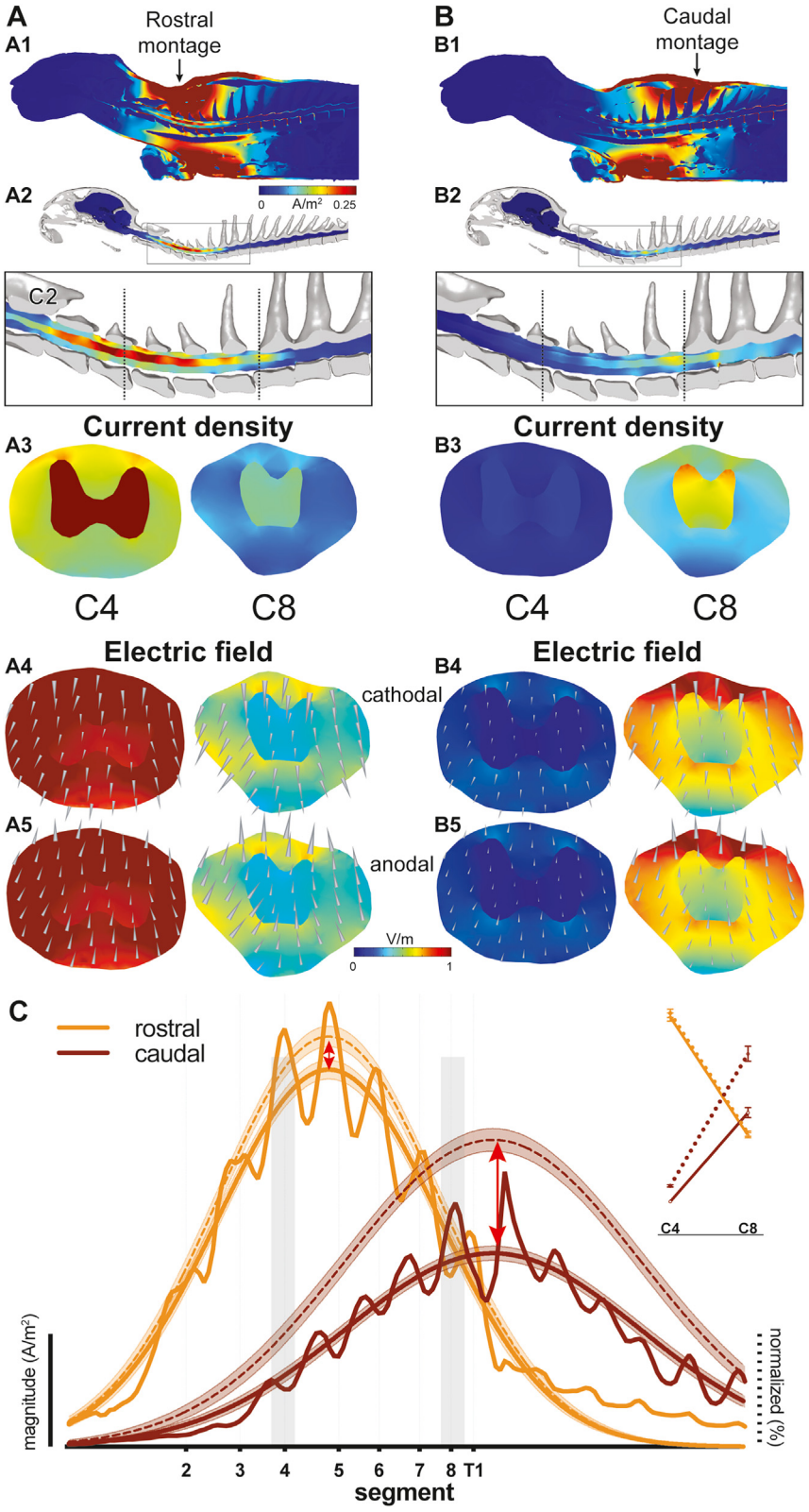

Fig. 6. Realistic whole-body computational maps of tsDCS current flow.
FEM model predictions of tsDCS current flow and electric field across tissue layers for the rostral (**A**) and the caudal (**B**) montages (colormap; low density = blue; high = red). The global (A1, B1) and intraspinal current flow from midsagittal (A2, B2) and transverse (A3, B3) slices (arrows in A1 and B1 point to the middle of the target electrodes; scales are the same in **A1-3** and **B1-3**). Current density is higher in the gray matter compared to white matter reflecting its lower resistivity. Maps of the electric field magnitude (A4,5; B4,5) on the transverse sections shown in A3 and B3 respectively. Electric field direction is represented by the cones. **C**. Distribution of current density in the cervicothoracic cord. The magnitude of current density shifts across the spinal axis and peaks between the intervertebral spaces (raw values on left y-axis; dark solid lines). Gaussian fit of the raw data (thick solid lines; ± 95% C.I.) is overlaid and the effect of normalization (red dimension lines) replotted on the right y-axis (dotted lines; ± 95% C.I.). The inset shows the segmental current density for the raw and normalized values (±SEM) at C4 and C8 (0.5 mm x 5 slices; shaded bars). (For interpretation of the references to color in this figure legend, the reader is referred to the Web version of this article.)

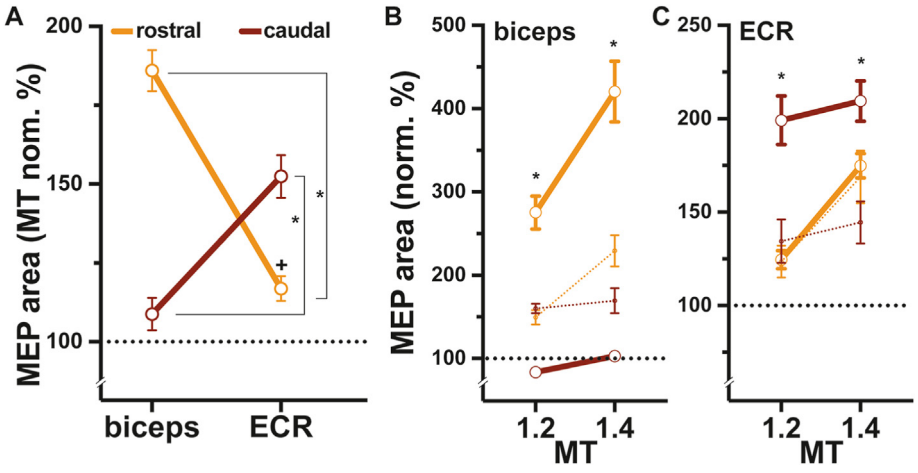

Fig. 7. Montage-dependent tsDCS modulation of MEP responses.
A. Effects of tsDCS-montage on MEP increases for biceps and ECR responses at motor threshold (MT). Rostral-tsDCS (orange) showed the largest MEP increase for the biceps whereas caudal-tsDCS (brown) showed the largest increase for the ECR ('+' indicates difference from baseline, '*' indicates difference between muscle groups; mean ± SEM). **B** and **C**. Effects on suprathreshold MEP recruitment (solid line) for biceps (B) and ECR (C) (recruitment baseline, colored dotted line) for each montage ['*' indicates difference between montage; mean ± SEM]. (For interpretation of the references to color in this figure legend, the reader is referred to the Web version of this article.)

the spinal cord; the absolute values remain the same. The magnitude of the field is represented by cones that are proportional (in size) to the electric field at the cone base. Due to its greater conductivity, the gray matter has a lower electric field than the white matter despite having a higher current density. However, direct comparisons between gray matter and white matter electric field should be cautioned because of potential differences in the excitability of those tissues.

Plotting the predicted rostro-caudal (i.e., axial) current density for the two montages (Fig. 6C) shows a current flow bias toward either rostral or caudal segments for the rostral and caudal-montages, respectively. The single large peaks for each montage on the Gaussian plots (see below) corresponds to the rostral cervical and caudal cervical-rostral thoracic current density 'hot spots.' The periodic peaks in current density, evident on the raw traces, correspond to the intervertebral spaces. There is an intersegmental reversal in rank order of the C4 and C8 targets between the rostral and caudal montage [Fig. 6C inset; $F_{(2,24)} = 454.70$, $P < 0.001$*]. The rostral montage had a larger rostro-caudal magnitude of the current density and electric field strength relation for intraspinal current than the caudal montage. This reflects scaling by stimulation intensity; we applied the same current for both montages despite less current flow through the upper trunk. Total spinal current flow across montages was fit to a Gaussian function (Fig. 6C, solid lines) and then scaled (i.e., normalized) to the mean (Fig. 6C, dashed lines). When the magnitude functions were normalized to each distribution mean, the reciprocal differences at C8 were larger (Fig. 6C inset, dotted lines).

3.6. Spinal cord neuromodulation of forelimb proximal and distal motor output is montage-specific

We next tested the hypothesis that the more rostral cathode montage would preferentially enhance biceps, whose motor pool is located rostrally, while the more caudal montage would preferentially enhance ECR, whose motor pool is located caudally. We recorded threshold MEPs for each location and compared responses during 4 mA tsDCS. For the rostral montage, there was stronger potentiation of biceps than ECR MEPs with motor threshold testing; whereas for the caudal montage, there was strong potentiation of ECR MEPs but no change in biceps (Fig. 7A, '+' indicates difference from baseline, Bonferroni corrected). The level of MEP potentiation with rostral 4 mA tsDCS was smaller for the biceps in the intensity group (59%; Fig. 3C) compared to the montage group (86%) [unpaired $t_{(182)} = 2.45$, $P < 0.02$]. There was no difference for ECR responses between the intensity (29%; Fig. 3D) and montage (17%) studies [unpaired $t_{(182)} = 1.63$, $P = 0.10$]. This double dissociation of cathode location (rostral or caudal) and dominant muscle response (biceps or ECR) parallels the model's prediction (Fig. 6C inset).

We next determined if the differential neuromodulatory effects of cathode location affected the capacity to recruit larger MEPs with stronger cortical stimuli. Recruitment reveals the capacity for a progressively greater corticospinal descending drive to activate muscle [48–50]. For biceps, the rostral montage enhanced recruitment; the caudal montage was ineffective [Fig. 7B, two-way $_{interaction}F_{(2,351)} = 5.99$, $P < 0.001$*; $_{montage}F_{(1,351)} = 75.96$, $P < 0.001$*; Holm-Sidak: Rostral > Caudal]. For ECR, the caudal montage was much more effective than the rostral electrode in enhancing recruitment [Fig. 7C, two-way $_{interaction}F_{(2,360)} = 3.52$, $P < 0.001$*; $_{montage}F_{(1,360)} = 50.42$, $P < 0.001$*; Holm-Sidak: rostral < caudal]. Biceps increases were greater with the rostral position using 1.2 and 1.4 MT compared to ECR, and the reverse was true for the caudal (Welch's multiple comparisons with Holm-Sidak correction). These findings show that cathodal tsDCS can enhance biceps or ECR responses with montage-selective targeting which associates with the rostrocaudal distributions of their motoneuron pools.

4. Discussion

In this translational study, we developed a framework for the rational design and testing of tsDCS interventions—including the use of acute MEP changes as an immediate biomarker of corticospinal modulation and integrating segmental FEM current flow models with rostrocaudal motor pool representations. The model has enhanced spatial features compared with prior studies, including co-registration of high-resolution MRI and CT, which are optimal to resolve soft and ossified tissues, respectively. MRI and CT were from post-mortem specimens, which eliminate movement artifacts. We show that non-invasive tsDCS can facilitate corticospinal drive for one muscle preferentially over another, depending on electrode location, showing targeting of tsDCS intervention. We identified an anatomical association between MEP selectivity

and motor pool rostrocaudal location. Computational modeling informed an anatomical mechanism for this selectivity, whereby the cathode location that was effective for MCX-evoked biceps (proximal muscle) activation steered more current rostrally in the cervical cord, and the location effective for ECR (distal muscle) activation steered more current caudally. Clinical effectiveness and mechanism-driven therapy depends on methods to guide tsDCS to target motor functions. The framework we developed provides a path to achieve and optimize motor specific responses to help guide tsDCS neurorehabilitation after injury.

4.1. Montage focality reveals that motoneurons are a target of tsDCS action

Consistent with other studies [13], cathodal tsDCS enhancement and anodal suppression of corticospinal output did not require substantial time to build (i.e., no wind-up period). This rapid response is more consistent with a direct action on ionic fluxes determining neuronal excitability [30] than long-term plasticity, which has been suggested for tDCS [51]. It is well established that direct current application within the spinal cord immediately polarizes afferent fiber terminals and modulates 1A afferent EPSPs into motoneurons [19,52–54]. Cervical c- and a-tsDCS in rats both induce immediate enhancement of spontaneous forelimb motor unit firing during stimulation, albeit cathodal greater than anodal [30]. Only c-tsDCS produced persistent enhancement in spontaneous motor unit firing, an excitability change that is abrogated by voltage-gated Ca2+ channel blockade, suggesting activation of a motoneuron persistent inward current (PIC) [30]. The high density of voltage-gated Ca^{2+} channels in motoneuron dendrites and the extensive dendritic arbor [55–58] may confer higher sensitivity of motoneurons to tsDCS than other neuron types. Differential response to cathodal versus anodal tsDCS may be explained by non-linear and spatial motoneuron properties, including the non-linear characteristic of motoneuron membrane channels [56]; proximity to the current source, and the orientation of the dendritic arbor, which governs the amount and direction of membrane polarization [55]. However, the neurophysiological consequences of tsDCS polarity will depend on network connectivity—including inhibitory neuron function—as well as state, which are complex to consider. The association between montage-specificity and motor pool locations, with a higher density of biceps motoneurons in rostral segments and ECR motoneurons, caudally [47], support spinal motoneurons as a target of tsDCS and can explain the regional extent, or 'receptive field,' of tsDCS neuromodulation on corticospinal drive.

4.2. Modulation of descending MCX signaling

The MCX acts on spinal motoneurons through monosynaptic and oligosynaptic spinal interneuronal paths and via brain stem projections in a species-dependent manner (e.g., corticoreticulospinal tract) [1]. Whereas in humans and many non-human primate species monosynaptic connections are present, in the cat the shortest CST-to-motoneuron path is disynaptic [59]. MCX stimulation and voluntary muscle recruitment can produce muscle responses through any or all of these routes [60,61]. Moreover, descending cortical signaling may preferentially activate reticulospinal than corticospinal tracts after SCI due to corticospinal tract axon loss and reticulospinal axon sparing and plasticity [62,63]. In addition to motoneurons themselves, two features of the spinal underpinnings of proximal-distal muscle control that have a rostro-caudal organization may be affected differently by tsDCS. First, propriospinal and segmental interneurons—which are located rostrally and caudally, respectively—differentially control proximal and distal muscle synergies [64]. These interneuron classes have been identified in humans [65,66]. This differential organization and susceptibility to neuromodulation is reminiscent of the effects of cerebellar tDCS, which can modulate task-dependent adaptation of arm/proximal movements; whereas motor cortex tDCS modulates adaptation of finger/hand movements [67]. Tapping differentially into proximal and distal control circuits, or other motor synergies, may engage underlying spinal circuitry for motor control [68]. Second, MCX elbow flexor and wrist joint zones have distinctive anatomical terminations in the rostral and caudal cervical cord and, in turn, differential access to premotor interneurons [69]. The rostral and caudal cathodal positions could differentially target proximal and distal control circuits. Our approach suggests that it is necessary to integrate segmental current flow maps (from FEM simulations) with segmental representations of the postulated neuronal element targeted (e.g., motoneurons, interneurons, or fibers), to predict differential actions of tsDCS montages that enhance motor-specific interventions.

5. Conclusions

tsDCS is well-suited for use as a personalized therapy, including in neurorehabilitation following injury. It is non-invasive and, we show, can be MEP response selective. Three results of our study would benefit human translation. First, image-based modeling could be used to target segmental regions, similar to empirical targeting of muscle effects in epidural spinal stimulation. This is particularly important for spinal stimulation because of the complex and segmental structural differences of the vertebra between individuals (and across species), with low-impedance current entry zones and segmental localization of motor circuits. Second, the use of a clinically-based physiological biomarker for efficacy—MEP facilitation during stimulation—in conjunction with scaled estimates of necessary currents provide rapid outcome feedback for within-session optimization. Third, consider sampling multiple muscle groups concurrently to yield a receptive field for effective neuromodulation and input-output relations, given our demonstration of montage-specific motor effects and non-linearities in threshold.

Funding

This work was supported by the New York State Spinal Cord Injury Board (JHM: DOH01-C31291GG).

CRediT authorship contribution statement

Preston T.J.A. Williams: Conceptualization, Methodology, Validation, Formal analysis, Investigation, Writing – original draft, Writing – review & editing, Visualization. **Dennis Q. Truong:** Methodology, Software, Formal analysis, Investigation, Data curation. **Alan C. Seifert:** Investigation, Writing – review & editing. **Junqian Xu:** Investigation, Resources, Writing – review & editing. **Marom Bikson:** Conceptualization, Resources, Writing – review & editing. **John H. Martin:** Conceptualization, Methodology, Investigation, Writing – original draft, Writing – review & editing, Visualization, Supervision, Project administration, Funding acquisition.

Acknowledgements

We express gratitude to Xiuli Wu for histological preparations; Adrish Sarkar for segmentation assistance; Mr. Harry Acosta and Dr. Sulli Popilskis for veterinary care.

References

[1] Lemon RN. Descending pathways in motor control. Annu Rev Neurosci 2008;31:195–218.
[2] Martin JH. The corticospinal system: from development to motor control. Neuroscientist 2005;11:161–73.
[3] Jack AS, Hurd C, Martin J, Fouad K. Electrical stimulation as a tool to promote plasticity of the injured spinal cord. J Neurotrauma 2020;37(18):1933–53.
[4] Talelli P, Greenwood RJ, Rothwell JC. Arm function after stroke: neurophysiological correlates and recovery mechanisms assessed by transcranial magnetic stimulation. Clin Neurophysiol 2006;117(8):1641–59.
[5] Oudega M, Perez MA. Corticospinal reorganization after spinal cord injury. J Physiol 2012;590(Pt 16):3647–63.
[6] Carmel JB, Berrol LJ, Brus-Ramer M, Martin JH. Chronic electrical stimulation of the intact corticospinal system after unilateral injury restores skilled locomotor control and promotes spinal axon outgrowth. J Neurosci 2010;30(32):10918–26.
[7] Nudo RJ, Jenkins WM, Merzenich MM. Repetitive microstimulation alters the cortical representation of movements in adult rats. Somatosens Mot Res 1990;7(4):463–83.
[8] Zareen N, Dodson S, Armada K, Awad R, Sultana N, Hara E, et al. Stimulation-dependent remodeling of the corticospinal tract requires reactivation of growth-promoting developmental signaling pathways. Exp Neurol 2018;307:133–44.
[9] Edgerton VR, Leon RD, Harkema SJ, Hodgson JA, London N, Reinkensmeyer DJ, et al. Retraining the injured spinal cord. J Physiol 2001;533(Pt 1):15–22.
[10] Rejc E, Angeli CA, Bryant N, Harkema SJ. Effects of stand and step training with epidural stimulation on motor function for standing in chronic complete paraplegics. J Neurotrauma 2017;34(9):1787–802. https://doi.org/10.1089/neu.2016.4516.
[11] Song W, Martin JH. Spinal cord direct current stimulation differentially modulates neuronal activity in the dorsal and ventral spinal cord. J Neurophysiol 2017;117(3):1143–55.
[12] Song W, Truong DQ, Bikson M, Martin JH. Transspinal direct current stimulation immediately modifies motor cortex sensorimotor maps. J Neurophysiol 2015;113(7):2801–11.
[13] Ahmed Z. Trans-spinal direct current stimulation modulates motor cortex-induced muscle contraction in mice. J Appl Physiol 2011;110(5):1414–24.
[14] Donges SC, Bai S, Taylor JL. Concurrent electrical cervicomedullary stimulation and cervical transcutaneous spinal direct current stimulation result in a stimulus interaction. Exp Physiol 2017;102(10):1309–20.
[15] Fernandes SR, Pereira M, Salvador R, Miranda PC, de Carvalho M. Cervical trans-spinal direct current stimulation: a modelling-experimental approach. J NeuroEng Rehabil 2019;16(1):123.
[16] Cogiamanian F, Ardolino G, Vergari M, Ferrucci R, Ciocca M, Scelzo E, et al. Transcutaneous spinal direct current stimulation. Front Psychiatr 2012;3:63.
[17] Yamaguchi T, Beck MM, Therkildsen ER, Svane C, Forman C, Lorentzen J, et al. Transcutaneous spinal direct current stimulation increases corticospinal transmission and enhances voluntary motor output in humans. Phys Rep 2020;8(16):e14531.
[18] Nitsche MA, Paulus W. Excitability changes induced in the human motor cortex by weak transcranial direct current stimulation. J Physiol 2000;527(Pt 3):633–9.
[19] Jankowska E. Spinal control of motor outputs by intrinsic and externally induced electric field potentials. J Neurophysiol 2017;118(2):1221–34.
[20] Knikou M, Dixon L, Santora D, Ibrahim MM. Transspinal constant-current long-lasting stimulation: a new method to induce cortical and corticospinal plasticity. J Neurophysiol 2015;114(3):1486–99.
[21] Song W, Amer A, Ryan D, Martin JH. Combined motor cortex and spinal cord neuromodulation promotes corticospinal system functional and structural plasticity and motor function after injury. Exp Neurol 2016;277:46–57.
[22] Bolzoni F, Baczyk M, Jankowska E. Subcortical effects of transcranial direct current stimulation in the rat. J Physiol 2013;591(16):4027–42.
[23] Baczyk M, Pettersson LG, Jankowska E. Facilitation of ipsilateral actions of corticospinal tract neurons on feline motoneurons by transcranial direct current stimulation. Eur J Neurosci 2014;40(4):2628–40.
[24] Niérat M-C, Similowski T, Lamy J-C. Does trans-spinal direct current stimulation alter phrenic motoneurons and respiratory neuromechanical outputs in humans? A double-blind, sham-controlled, randomized, crossover study. J Neurosci 2014;34(43):14420–9.
[25] Baczyk M, Drzymala-Celichowska H, Mrowczynski W, Krutki P. Motoneuron firing properties are modified by trans-spinal direct current stimulation in rats. J Appl Physiol 1985;126(5):1232–41. 2019.
[26] Baczyk M, Drzymala-Celichowska H, Mrowczynski W, Krutki P. Polarity-dependent adaptations of motoneuron electrophysiological properties after 5-wk transcutaneous spinal direct current stimulation in rats. J Appl Physiol 1985;129(4):646–55. 2020.
[27] Ahmed Z. Modulation of gamma and alpha spinal motor neurons activity by trans-spinal direct current stimulation: effects on reflexive actions and locomotor activity. Phys Rep 2016;4(3).
[28] Huang Y, Liu AA, Lafon B, Friedman D, Dayan M, Wang X, et al. Measurements and models of electric fields in the in vivo human brain during transcranial electric stimulation. Elife 2017;6.
[29] Jackson MP, Rahman A, Lafon B, Kronberg G, Ling D, Parra LC, et al. Animal models of transcranial direct current stimulation: methods and mechanisms. Clin Neurophysiol 2016;127(11):3425–54.
[30] Song W, Martin JH. Trans-spinal direct current stimulation targets Ca2+ channels to induce persistent motor unit responses. Front Neurosci 2022;16. https://doi.org/10.3389/fnins.2022.856948.
[31] Peterchev AV, Wagner TA, Miranda PC, Nitsche MA, Paulus W, Lisanby SH, et al. Fundamentals of transcranial electric and magnetic stimulation dose: definition, selection, and reporting practices. Brain Stimul 2012;5(4):435–53.
[32] Datta A, Zhou X, Su Y, Parra LC, Bikson M. Validation of finite element model of transcranial electrical stimulation using scalp potentials: implications for clinical dose. J Neural Eng 2013;10(3):036018.
[33] Parazzini M, Fiocchi S, Liorni I, Rossi E, Cogiamanian F, Vergari M, et al. Modeling the current density generated by transcutaneous spinal direct current stimulation (tsDCS). Clin Neurophysiol 2014;125(11):2260–70.
[34] Chakrabarty S, Martin JH. Postnatal development of the motor representation in primary motor cortex. J Neurophysiol 2000;84:2582–94.
[35] Wongsarnpigoon A, Grill WM. Effects of stimulation parameters and electrode location on thresholds for epidural stimulation of cat motor cortex. J Neural Eng 2011;8(6):066016.
[36] Armstrong DM, Drew T. Electromyographic responses evoked in muscles of the forelimb by intracortical stimulation in the cat. J Physiol 1985;367:309–26.
[37] Williams PTJA, Truong DQ, De Paolis A, Ryan D, Smith MD, Alexander H, Wong J, Ambia S, Cardoso L, Bikson M, Martin JH. Augmenting corticospinal system output in a pre-clinical large animal model of cervical contusion injury with combined brain and spinal cord stimulation. Chicago, IL: Society for Neuroscience; 2019.
[38] Yang Q, Ramamurthy A, Lall S, Santos J, Ratnadurai-Giridharan S, Lopane M, et al. Independent replication of motor cortex and cervical spinal cord electrical stimulation to promote forelimb motor function after spinal cord injury in rats. Exp Neurol 2019;320:112962.
[39] Williams PT, Kim S, Martin JH. Postnatal maturation of the red nucleus motor map depends on rubrospinal connections with forelimb motor pools. J Neurosci 2014;34(12):4432–41.
[40] Mohan R, Tosolini AP, Morris R. Targeting the motor end plates in the mouse hindlimb gives access to a greater number of spinal cord motor neurons: an approach to maximize retrograde transport. Neuroscience 2014;274:318–30.
[41] Rahman A, Reato D, Arlotti M, Gasca F, Datta A, Parra LC, et al. Cellular effects of acute direct current stimulation: somatic and synaptic terminal effects. J Physiol 2013;591(Pt 10):2563–78.
[42] Toshev PK, Guleyupoglu B, Bikson M. Informing dose design by modeling transcutaneous spinal direct current stimulation. Clin Neurophysiol 2014;125(11):2147–9.
[43] Zareen N, Shinozaki M, Ryan D, Alexander H, Amer A, Truong DQ, et al. Motor cortex and spinal cord neuromodulation promote corticospinal tract axonal outgrowth and motor recovery after cervical contusion spinal cord injury. Exp Neurol 2017;297:179–89.
[44] Huang Y, Thomas C, Datta A. Optimized transcutaneous spinal cord direct current stimulation using multiple electrodes from 3/9/7 system. Annu Int Conf IEEE Eng Med Biol Soc 2019;2019:6290–3.
[45] Kuck A, Stegeman DF, van Asseldonk EHF. Modeling trans-spinal direct current stimulation in the presence of spinal implants. IEEE Trans Neural Syst Rehabil Eng 2019;27(5):790–7.
[46] Bikson M, Rahman A, Datta A. Computational models of transcranial direct current stimulation. Clin EEG Neurosci 2012;43(3):176–83.
[47] Sterling P, Kuypers HG. Anatomical organization of the brachial spinal cord of the cat. II. The motoneuron plexus. Brain Res 1967;4(1):16–32.
[48] Bawa P, Lemon RN. Recruitment of motor units in response to transcranial magnetic stimulation in man. J Physiol 1993;471:445–64.
[49] Davey NJ, Smith HC, Savic G, Maskill DW, Ellaway PH, Frankel HL. Comparison of input-output patterns in the corticospinal system of normal subjects and incomplete spinal cord injured patients. Exp Brain Res 1999;127(4):382–90.
[50] Devanne H, Lavoie BA, Capaday C. Input-output properties and gain changes in the human corticospinal pathway. Exp Brain Res 1997;114(2):329–38.
[51] Cirillo G, Di Pino G, Capone F, Ranieri F, Florio L, Todisco V, et al. Neurobiological after-effects of non-invasive brain stimulation. Brain Stimul 2017;10(1):1–18.
[52] Kaczmarek D, Ristikankare J, Jankowska E. Does trans-spinal and local DC polarization affect presynaptic inhibition and post-activation depression? J Physiol 2017;595(5):1743–61.
[53] Bolzoni F, Jankowska E. Presynaptic and postsynaptic effects of local cathodal DC polarization within the spinal cord in anaesthetized animal preparations. J Physiol 2015;593(4):947–66.
[54] Bolzoni F, Esposti R, Bruttini C, Zenoni G, Jankowska E, Cavallari P. Direct current stimulation modulates the excitability of the sensory and motor fibres in the human posterior tibial nerve, with a long-lasting effect on the H-reflex. Eur J Neurosci 2017;46:2499–506.
[55] Elbasiouny SM, Mushahwar VK. Suppressing the excitability of spinal motoneurons by extracellularly applied electrical fields: insights from computer simulations. J Appl Physiol 1985;103(5):1824–36. 2007.
[56] Kurian M, Crook SM, Jung R. Motoneuron model of self-sustained firing after spinal cord injury. J Comput Neurosci 2011;31(3):625–45.

[57] Balaskas N, Abbott LF, Jessell TM, Ng D. Positional strategies for connection specificity and synaptic organization in spinal sensory-motor circuits. Neuron 2019;102(6):1143–11456 e4.
[58] Hounsgaard J, Hultborn H, Jespersen B, Kiehn O. Bistability of alpha-motoneurones in the decerebrate cat and in the acute spinal cat after intravenous 5-hydroxytryptophan. J Physiol 1988;405:345–67.
[59] Porter R, Lemon R. Corticospinal function and voluntary movement. Oxford: Oxford Science; 1993.
[60] Baker SN, Zaaimi B, Fisher KM, Edgley SA, Soteropoulos DS. Pathways mediating functional recovery. Prog Brain Res 2015;218:389–412.
[61] Baker SN, Perez MA. Reticulospinal contributions to gross hand function after human spinal cord injury. J Neurosci 2017;37(40):9778–84.
[62] Sangari S, Perez MA. Imbalanced corticospinal and reticulospinal contributions to spasticity in humans with spinal cord injury. J Neurosci 2019;39(40):7872–81.
[63] Ballermann M, Fouad K. Spontaneous locomotor recovery in spinal cord injured rats is accompanied by anatomical plasticity of reticulospinal fibers. Eur J Neurosci 2006;23(8):1988–96.
[64] Alstermark B, Isa T, Pettersson LG, Sasaki S. The C3-C4 propriospinal system in the cat and monkey: a spinal pre-motoneuronal centre for voluntary motor control. Acta Physiol 2007;189(2):123–40.
[65] Pierrot-Deseilligny E. Transmission of the cortical command for human voluntary movement through cervical propriospinal premotoneurons. Prog Neurobiol 1996;48(4–5):489–517.
[66] Pierrot-Deseilligny E, Burke D. The circuitry of the human spinal cord. Cambridge, UK: Cambridge University Press; 2005.
[67] Weightman M, Brittain JS, Punt D, Miall RC, Jenkinson N. Targeted tDCS selectively improves motor adaptation with the proximal and distal upper limb. Brain Stimul 2020;13(3):707–16.
[68] Yang Q, Logan D, Giszter SF. Motor primitives are determined in early development and are then robustly conserved into adulthood. Proc Natl Acad Sci U S A 2019;116(24):12025–34.
[69] Asante CO, Martin JH. Differential joint-specific corticospinal tract projections within the cervical enlargement. PLoS One 2013;8(9):e74454.